










In the format provided by the authors and unedited.

# Attosecond optical-field-enhanced carrier injection into the GaAs conduction band

F. Schlaepfer <sup>1\*</sup>, M. Lucchini <sup>1,3</sup>, S. A. Sato <sup>2</sup>, M. Volkov <sup>1</sup>, L. Kasmi <sup>1</sup>, N. Hartmann <sup>1</sup>,  
A. Rubio <sup>2</sup>, L. Gallmann <sup>1</sup> and U. Keller <sup>1\*</sup>

---

<sup>1</sup>Department of Physics, ETH Zurich, Zurich, Switzerland. <sup>2</sup>Max Planck Institute for the Structure and Dynamics of Matter, Hamburg, Germany. <sup>3</sup>Present address: Department of Physics, Politecnico di Milano, Milano, Italy. \*e-mail: [f.schlaepfer@phys.ethz.ch](mailto:f.schlaepfer@phys.ethz.ch); [keller@phys.ethz.ch](mailto:keller@phys.ethz.ch)

# Attosecond optical-field-enhanced carrier injection into the GaAs conduction band

F. Schlaepfer,<sup>1\*</sup> M. Lucchini,<sup>1†</sup> S. A. Sato,<sup>2</sup> M. Volkov,<sup>1</sup> L. Kasmi,<sup>1</sup>  
N. Hartmann,<sup>1</sup> A. Rubio,<sup>2</sup> L. Gallmann,<sup>1</sup> U. Keller<sup>1</sup>

<sup>1</sup>Department of Physics, ETH Zurich, 8093 Zurich, Switzerland

<sup>2</sup>Max Planck Institute for the Structure and Dynamics of Matter, Luruper Chaussee 149, 22761 Hamburg, Germany

\*To whom correspondence should be addressed;

†Current address: Department of Physics, Politecnico di Milano, 20133 Milano, Italy

E-mail: [f.schlaepfer@phys.ethz.ch](mailto:f.schlaepfer@phys.ethz.ch)

## S1 Experimental methods

### S1.1 Experimental Setup

The setup used for this experiment is shown in Fig. S1. A detailed description can be found in Ref. 19. We use a near-infrared (IR) beam from a commercial Ti-sapphire laser system with a repetition rate of 1 kHz and pulse duration of around 25 fs. The pulses are further compressed with a filament compressor to 5 to 6 fs. The center wavelength is around 780 nm and the average power 280 mW. The laser beam is divided with a beam splitter into two parts. 80% of the power propagates through a polarization gating (PG) setup<sup>31</sup> and is focused into a gas cell filled with argon for high harmonic generation (HHG). By adjusting the orientation of the birefringent crystals in the PG setup, either attosecond pulse trains (APTs) or single attosecond pulses (SAPs) are generated. An aluminum filter placed after the gas nozzle blocks the residual IR radiation used for HHG. The generated attosecond pulse with a spectrum in the extreme-ultraviolet energy

range (XUV) acts as the probe in the current pump-probe experiment. The IR beam reflected by the beam splitter (20%) follows a piezo-controlled delay path. This beam provides the IR pump pulse in our experiment. Both the pump and probe beams are  $p$  polarized. They are collinearly recombined with a center-hole mirror. The smaller XUV beam propagates through the hole while the IR is reflected on the outer part of the mirror. The two beams are then focused with a toroidal mirror into the double-target configuration consisting of a neon gas jet followed by a 100-nm thick single-crystalline GaAs membrane. This double-target enables both a streaking measurement in the Ne-target and an attosecond transient absorption spectroscopy (ATAS) measurement in the GaAs membrane. From the streaking trace, the temporal shape of the vector potential and electric field of the IR pump pulse can be reconstructed<sup>20,21</sup>. The spacing between the gas nozzle and GaAs membrane is 1.35 mm, which we took into account for the calibration of the pump-probe delay (see below in Section S1.6 for more details). This is necessary to study the sub-femtosecond timing of the electron dynamics in the sample.

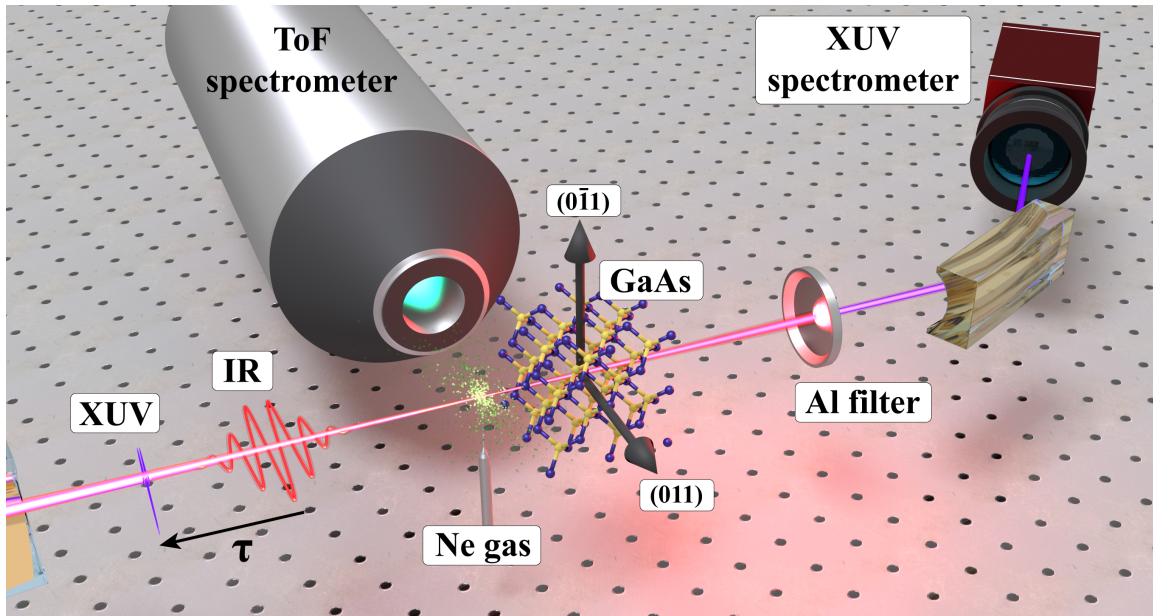


**Fig. S1. Experimental setup.** Sketch of pump-probe setup with the double-target configuration consisting of a gas nozzle (neon) followed by a 100-nm thick freestanding crystalline GaAs membrane. Both pulses are polarized along the (011) crystal orientation of GaAs. A positive delay means that the IR pulse arrives first and the XUV second.

Photoelectrons generated in the gas jet are measured with a time-of-flight spectrometer, while an XUV spectrometer with a resolution of  $\approx 70$  meV records the spectra of the probe pulses after transmission through the GaAs membrane. With the help of a fast

electronic shutter placed in the pump path (operation frequency up to 150 Hz), ATAS spectra without (reference) and with (signal) the presence of the pump pulse can be recorded in fast sequence.

### S1.2 IR-induced modification of the XUV absorption

The 2D-color plots with the measured data discussed in the main manuscript show the pump-induced change of the XUV absorption,  $\Delta Abs(E, \tau)$ , which can be expressed as

$$\begin{aligned} \Delta Abs(E, \tau) &= \Delta \alpha(E, \tau)L = \alpha_{IR}(E, \tau)L - \alpha_0(E)L \\ &= -\ln\left(\frac{I_{trans}^{sig}(E, \tau)}{I_{initial}(E)}\right) + \ln\left(\frac{I_{trans}^{ref}(E)}{I_{initial}(E)}\right) = \ln\left(\frac{I_{trans}^{ref}(E)}{I_{trans}^{sig}(E, \tau)}\right). \end{aligned} \quad (S1)$$

$\alpha_{IR}$  and  $\alpha_0$  describe the absorption per length  $L$  with the pump pulse on (signal) and off (reference), respectively.  $E$  denotes the photon energy.  $\tau$  is the delay between pump and probe pulses.  $I_{initial}$  is the initial XUV spectral intensity, while  $I_{trans}^{sig}$  and  $I_{trans}^{ref}$  are the transmitted XUV spectral intensities with and without the pump pulse. By recording signal and reference spectra in fast sequence, we can efficiently suppress slowly varying noise contributions and resolve changes in the XUV absorption of less than 1%.

### S1.3 Sample properties and preparation

The sample measured here is a freestanding single-crystalline GaAs membrane with a thickness of 100 nm. The illuminated top surface is the (100) plane. The linear pump and probe polarizations point both along the (011) crystal orientation, which means that we probe along the  $\Sigma$ -symmetry line in the reciprocal space.

The fabrication process of the nanomembrane involves a combination of mechanical polishing and chemical wet etching of a semiconductor heterostructure grown by molecular beam epitaxy (MBE)<sup>32,33</sup>. Both, growth and etching, were done in the clean room facility FIRST at ETH Zurich. The clear aperture of the membrane is around 0.4 x 0.6 mm. Due to the growth by MBE, we assume a uniform thickness and quality over the whole membrane. Nevertheless, the measurements have been repeated on different spots on two different samples to test the reproducibility of the experiment.

## S1.4 Infrared pulse parameters

Table S1 summarizes the parameters of the IR-pump pulse used for the measurement. A spectrum of the pulse is shown in Fig. 1 of the main manuscript. One can see that the pump is clearly in resonance with the bandgap of GaAs, which is at room temperature approximately  $1.42 \text{ eV}^{29}$ . The IR peak intensity and electric field strength have been estimated from the spatial and temporal profiles. These profiles have been obtained with a beam profiler camera and streaking measurements, respectively. Breakdown (laser induced damage) of the GaAs membrane was observed at a pulse energy of around  $2.25 \text{ }\mu\text{J}$  (corresponding to a peak intensity of approximately  $2.6 \times 10^{12} \text{ W/cm}^2$ ). The IR intensity inside the sample has been computed taking into account the dielectric function of GaAs<sup>34</sup> and the stationary solution of Maxwell's equations. The result gives a maximum intensity that changes along the beam propagation direction inside the sample and peaks at approximately 60% of the incident intensity. Therefore, the peak intensity of the pump inside the membrane is up to  $\approx 1.39 \times 10^{12} \text{ W/cm}^2$  and the peak electric field strength up to  $\approx 0.32 \text{ V/\AA}$ . Figure S2 shows the laser intensity dependence of the number of injected carriers from the VB into the CB computed by the first-principles calculation (see section S2). While the carrier population is proportional to the laser intensity in the weak intensity region, it shows a nonlinear response in the high intensity region. This result indicates that the injection mechanism in the current experiment is in the non-linear regime.

Energy	$\approx 2 \text{ }\mu\text{J}$
Pulse duration (FWHM)	$5.45 \pm 0.71 \text{ fs}$
Beam waist	$\approx 74.4 \text{ }\mu\text{m}$
Peak intensity	$(2.31 \pm 0.17) \times 10^{12} \text{ W/cm}^2$
Peak electric field strength	$0.42 \pm 0.02 \text{ V/\AA}$

**Tab. S1.** Laser parameters of the infrared pulse in vacuum. The intensity inside the membrane is up to 60% compared to the vacuum.

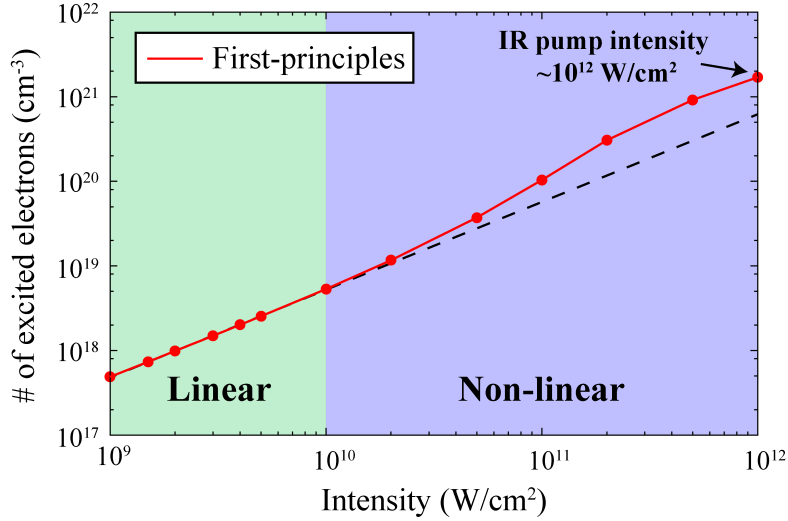


**Fig. S2. Injected carrier population vs. laser intensity.** For low pump intensities, a first-principles calculation predicts a linear relation between the number of carrier excited from the VB into the CB and the pump intensity. For intensities exceeding  $10^{10}$  W/cm<sup>2</sup>, the number of carriers deviates from the linear relation (black dashed line). Hence, in the current experiment with a pump intensity of  $\sim 10^{12}$  W/cm<sup>2</sup>, the carrier injection mechanism is in the non-linear regime.

### S1.5 Single attosecond pulse (SAP) vs. attosecond pulse train (APT)

The ATAS measurements shown in Fig. 2 of the main manuscript are measured with single attosecond pulses (SAPs). The temporal characterization of the SAP is obtained with the FROG-CRAB technique using the extended Ptychographic Iterative Engine (ePIE)<sup>35</sup>. In Fig. S3, a typical energy spectrum of a SAP together with its temporal reconstruction is shown. The pulse duration is approximately 200 as.

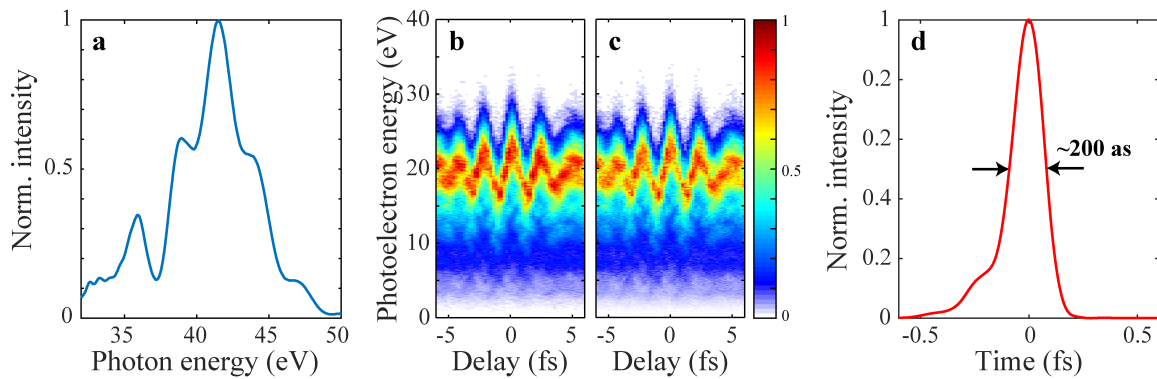


**Fig. S3. Single attosecond pulse (SAP) reconstruction.** (a) XUV spectrum. (b) Measured streaking trace. (c) Reconstructed streaking trace. (d) Reconstructed SAP.

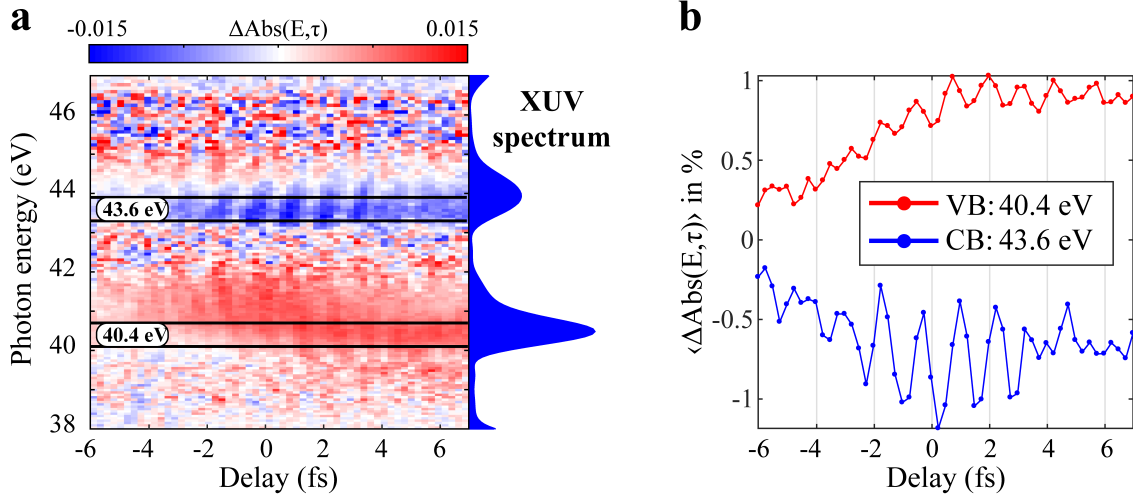


**Fig. S4. Attosecond transient absorption spectroscopy (ATAS) measurement performed with an attosecond pulse train (APT).** (a) ATAS trace with the corresponding XUV spectrum. (b) Energy averaged signal in the valence band (VB) (40.4 eV, red) and conduction band (CB) region (43.6 eV, blue). The integration intervals are shown in (a) with the black solid lines. The absorption change at 40.4 eV confirms the presence of  $2\omega_{IR}$ -oscillations also in the VB signal below 42 eV.

One advantage of using a SAP in the current experiment is the broad continuous spectrum, which makes it possible to study electron dynamics in the valence (VB) and conduction band (CB) at the same time. Compared to an APT however, SAPs are characterized by a lower photon flux and thus higher spectral noise. Due to the use of the PG technique, the SAPs used in our experiment are characterized by a strong dependence of the spectral amplitude around 40 eV on the carrier-envelope offset phase (CEP) of the driving pulses. Even if the CEP was actively stabilized to a *rms* value of  $< 0.15$  rad during the measurements, we were unable to resolve the characteristic oscillations in the transient absorption signal from the VB (in contrast to those at the higher photon energies probing the CB). Figure S4 shows a measurement with an APT, whose spectral amplitude does not depend on the IR CEP value. Here,  $2\omega_{IR}$ -oscillations are clearly visible both in the VB and in the CB (40.4 eV and 43.6 eV, respectively). This confirms the theoretical predictions reported in Fig. 2(c) of the main manuscript.

## S1.6 Pump-probe delay calibration

A precise pump-probe delay calibration is crucial for a comparison of the absolute phases of the absorption oscillations as discussed in Fig. 3(f) of the main manuscript. Figure S5(a) shows a typical streaking trace measured simultaneously with an ATAS trace. The negative vector potential  $-A(t)$  of the IR pulse follows approximately the center of mass (CM) of the streaking signal. In Fig. S5(b),  $A(t)^2$  is plotted together with the following fit function:

$$F(t) = \left( \left( a \cdot \cos(b \cdot (t - c) + d) \cdot \exp\left(-\frac{(t - c)^2}{2e^2}\right) \right) + f \right)^2, \quad (\text{S2})$$

where  $a$ ,  $b$ ,  $c$ ,  $d$ ,  $e$  and  $f$  are fitting parameters. We define delay zero as the local maximum closest to the maximum of the envelope.

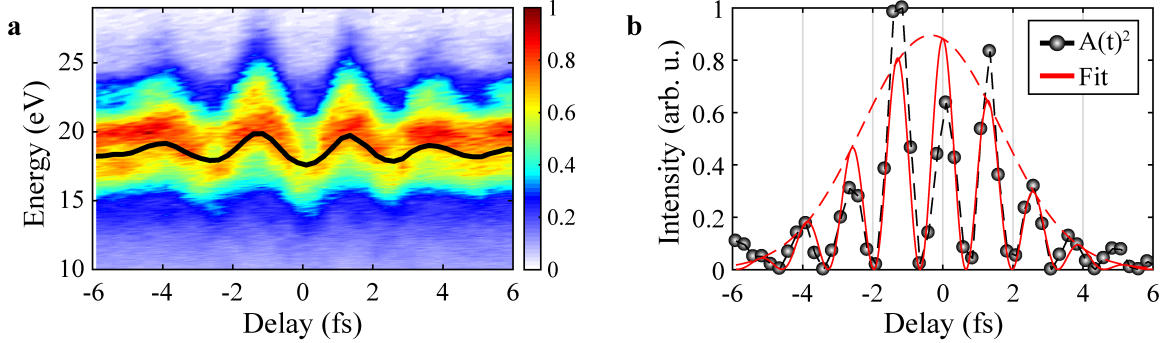


**Fig. S5. Delay calibration.** (a) Typical streaking trace measured simultaneously with the ATAS trace. The temporal shape of the vector potential  $A(t)$  follows the center of mass (black solid curve), but with opposite sign. (b) The black circles show the square of the extracted vector potential,  $A(t)^2$ , as extracted from (a). The amplitude mismatch between the experimental data and fit can be explained by the asymmetry in the streaking trace. Delay zero is defined as the local maximum of the fit (red line) being closest to the maximum of the envelope (red dashed line).

For the calibration of the timing between the pump and probe pulse, we take into account the following two issues:

### (1) Spatial separation between the streaking and ATAS target

In a recent publication, we demonstrated that the Gouy phase shift of the IR beam has a non-negligible influence onto attosecond pump-probe measurements with spatially separated targets<sup>22</sup>. In particular, for our focusing condition we found that the Gouy phase results in a phase shift for the IR beam of around minus 25 as/mm around the focus. In the experiment here, the spacing between the gas nozzle and GaAs membrane is



1.35 mm. Consequently, the IR electric field experiences a phase shift of minus  $\approx 34$  as while it propagates from the neon target to the GaAs membrane target.

*(2) Effect of the cross-section and atomic delay in the streaking reconstruction*

Above, we extracted the IR vector potential directly from the center of mass (CM) of the streaking without any reconstruction algorithm. Hence, the cross-section and atomic delay of the target gas are not taken into account. To estimate the error induced by this, we performed a simulation of a streaking trace and compared the input IR field  $E_{in}(t)$  with the reconstructed field defined as  $E_{rec}(t) \propto -\partial CM/\partial t$ . Including both the cross-section and atomic delay in the simulation results in a temporal offset between  $E_{in}(t)$  and  $E_{rec}(t)$  of  $\approx 30$  as. Hence, the reconstructed field defined as  $E_{rec}(t) \propto -\partial CM/\partial t$  has to be shifted by 30 as to positive delays to get the proper input field  $E_{in}(t)$ .

Both time shifts discussed above give a comparable but opposite shift to the IR pump field and therefore they practically cancel out. Therefore, in our analysis we took directly the CM extracted from the streaking trace without applying any further correction to reconstruct the IR vector potential ( $A(t) \propto -CM$ ).

**S1.7 Phase and delay extraction**

As discussed in the main manuscript, the phase of the absorption oscillations in the measured and simulated ATAS traces depends strongly on the photon energy  $E$  of the XUV pump pulse, which results in the tilted features in the signal. We extract the phase and delay between the squared vector potential of the IR pulse ( $S_1(t) = A(t)^2$ ) and the ATAS oscillation ( $S_2(E, t) = ATAS(E, t)$ ) for each XUV photon energy by looking at the following product, as in Ref. <sup>22</sup>:

$$C(E, \omega) = \tilde{S}_1(\omega) \cdot \tilde{S}_2(E, \omega)^*, \tag{S3}$$

where  $\tilde{S}_1(\omega)$  is the Fourier transform of  $S_1(t)$  and  $\tilde{S}_2(E, \omega)^*$  is the complex conjugate of the Fourier transform of  $S_2(E, t)$ .  $|C(E, \omega)|$  has a peak at the shared oscillation frequency of the two signals, which is equal to twice the IR frequency (Fig. S6). The phase of  $C$ , instead, gives the phase difference between  $S_1$  and  $S_2$ ,  $\Delta\Phi(E, \omega)$ . Hence, the relative phase offset between local maxima of the squared vector potential and the maxima of the

induced absorption modulation is extracted without any time-zero calibration. This avoids introducing an uncertainty in the phase difference through an uncertainty in the delay calibration. Finally, the energy dependence of the delay between the squared IR vector potential and the ATAS oscillations can be calculated as:

$$\langle \tau(E) \rangle = \frac{\int I(E, \omega) \cdot \frac{\Delta \Phi(E, \omega)}{\omega} d\omega}{\int I(E, \omega) d\omega}, \quad (\text{S4})$$

$$\sigma_{\langle \tau \rangle}^2(E) = \frac{\int I(E, \omega) \cdot \left[ \frac{\Delta \Phi(E, \omega)}{\omega} - \langle \tau(E) \rangle \right]^2 d\omega}{\int I(E, \omega) d\omega}. \quad (\text{S5})$$

Here,  $I(E, \omega)$  is a weighting function, equal to a Gaussian fit of  $|C(E, \omega)|$  within its full-width-at-half-maximum around the peak (Fig. S6). Equations (S4) and (S5) represent the delay and second momentum extracted from a single measurement/simulation.

The experimental delay in Fig. 3 of the main manuscript shows the statistical average of nine measurements recorded on four different days. The average experimental delay is calculated as follows:

$$\tau_{\text{average}}(E) = \frac{\sum_{i=1}^N \sigma_{\langle \tau_i \rangle}^{-2}(E) \cdot \langle \tau_i(E) \rangle}{\sum_{i=1}^N \sigma_{\langle \tau_i \rangle}^{-2}(E)}, \quad (\text{S6})$$

where  $\langle \tau_i(E) \rangle$  and  $\sigma_{\langle \tau_i \rangle}(E)$  represents the delay and uncertainty of the individual measurements and  $N$  the number of measurements. The error bar of the presented experimental delay is:

$$\delta \tau_{\text{average}}(E) = \sqrt{\frac{N}{N-1} \frac{\sum_{i=1}^N \sigma_{\langle \tau_i \rangle}^{-2}(E) \cdot \left| \langle \tau_i(E) \rangle - \tau_{\text{average}}(E) \right|^2}{\sum_{i=1}^N \sigma_{\langle \tau_i \rangle}^{-2}(E)} + \left( \frac{\sum_{i=1}^N \sigma_{\langle \tau_i \rangle}^{-1}(E)}{\sum_{i=1}^N \sigma_{\langle \tau_i \rangle}^{-2}(E)} \right)^2}. \quad (\text{S7})$$

The first term in the square root is the weighted variance of the nine individual delays  $\langle \tau_i(E) \rangle$  with respect to  $\tau_{\text{average}}(E)$ . The second term is the weighted mean of the individual uncertainties  $\sigma_{\langle \tau_i \rangle}(E)$ .

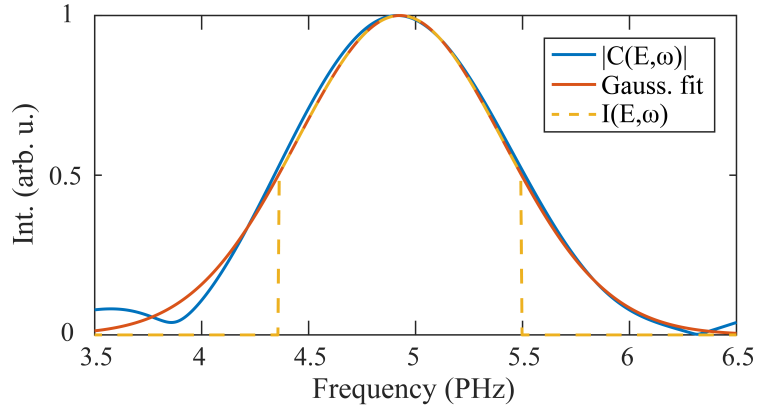


**Fig. S6. Phase and delay extraction.** The blue curve illustrates  $|C(E, \omega)|$  extracted from a simultaneously recorded streaking and ATAS trace ( $E = 46.6$  eV).  $|C(E, \omega)|$  has a peak at the common oscillation frequency of the squared IR field and ATAS trace ( $\omega_{peak} \approx 2\omega_{IR}$ ). The red curve is a Gaussian fit of  $|C(E, \omega)|$ . The weighting function  $I(E, \omega)$  used in Eqs. (S4) and (S5) is equal to the Gaussian fit within its full-width-at-half-maximum (FWHM) window (yellow curve).

## S2 Theoretical methods

In order to gain insights into the underlying physical dynamics for the observed features in the experiment, we employ two different theoretical models: (1) An *ab-initio* model based on first-principles density functional calculations and (2) a simplified three-band model. In this section, we briefly introduce both models and explain the simulation results.

### S2.1 First-principles electron dynamics simulation in the time-domain

To simulate the optical response of GaAs from first-principles, we solve the following one-body Schrödinger equation in the time-domain,

$$i\hbar \frac{\partial}{\partial t} u_{bk}(\mathbf{r}, t) = \left[ \frac{1}{2m} \left\{ \mathbf{p} + \hbar\mathbf{k} + \frac{e}{c} \mathbf{A}(t) \right\}^2 + v(\mathbf{r}) \right] u_{bk}(\mathbf{r}, t), \quad (\text{S8})$$

where  $u_{bk}(\mathbf{r}, t)$  describes the Bloch orbital with the band index  $b$  and crystal momentum  $\hbar\mathbf{k}$ . The one-body potential  $v(\mathbf{r})$  is approximated by the Kohn-Sham potential in the static density functional theory (DFT). Thus, equation (S8) is nothing but the time-dependent Kohn-Sham equation of the time-dependent density functional theory (TDDFT)<sup>36</sup> with frozen Hartree and exchange-correlation potentials.

In more detail, we perform a DFT calculation with a pseudopotential-based real-space TDDFT code (*Ab-initio* Real-Time Electron Dynamics simulator; ARTED<sup>37</sup>) to construct the one-body potential  $v(\mathbf{r})$ . We treat  $3d$ ,  $4s$ , and  $4p$  electrons of the Ga and As atoms as valence electrons. The exchange-correlation potential in the DFT calculation is given by a meta-GGA potential<sup>38</sup> with an optimized mixing-parameter,  $c$ , to reproduce the bandgap of GaAs at zero Kelvin<sup>39</sup>. In the experiment, the GaAs membrane is at room temperature and has therefore a reduced bandgap due to phononic effects. In the simulations however, we completely freeze the ions. Thus, to keep the treatment for electrons and phonons consistent, we consider the zero-temperature properties in the simulations for both.

Based on the above *ab-initio* modeling, we perform pump-probe simulations<sup>24</sup> and compute the transient modification of the imaginary part of the dielectric function,

$\text{Im}(\Delta\epsilon)$ , which is directly related to a change in the absorption<sup>10</sup>. We use a pump pulse with a peak electric field strength of  $2.75 \times 10^9$  V/m, a mean frequency of  $1.55$  eV/ $\hbar$  and a pulse width of about 5 fs. For the probe pulse, we set the peak field strength to  $2.75 \times 10^8$  V/m, the mean frequency to  $40$  eV/ $\hbar$  and the pulse duration to 250 as.

For the simulations in this paper, we employ a primitive unit cell of GaAs, which consists of a single Ga and As pair. We discretize the Brillouin zone into  $12^3$   $k$ -points. As in the experimental setup, the polarization of the pump and probe pulses are along the (011) crystal orientation. To numerically solve equation (S8) in the time-domain, we employ a basis expansion method with eigenstates of the static Kohn-Sham Hamiltonian using the momentum-shift technique<sup>40</sup>.

As mentioned in the main manuscript, we applied an energy shift of 4.23 eV to the first-principles results. The reason for this shift is due to the fact that the TDDFT calculation underestimates the energy gap between the core level and the top of the valence band. In our specific case, the simulated transition energy is 36.5 eV instead of 40.73 eV<sup>30</sup>. We corrected for this underestimation by shifting the absorption signal by 4.23 eV.

## S2.2 Role of the propagation effect

The frequency dependence of the refractive index of GaAs results in a different propagation speed of the IR-pump and XUV-probe pulse. The phase velocity of the IR pulse is about  $v_{IR} = c/n_{IR} \approx c/3.7$ <sup>34</sup>, where  $c$  describes the speed of light in vacuum. For a 100-nm thick GaAs membrane, the resulting propagation time for the pump pulse is about 1.233 fs. By assuming that the group velocity of the XUV pulse inside the bulk does not change much compared to the vacuum, the travel time of the probe is about 0.333 fs. Two pulses with an initial delay of zero femtosecond are therefore temporally separated by 900 as after the GaAs membrane. Consequently, the ATAS signal measured for a certain delay  $\tau$  is actually a signal averaged over pump-probe delays between  $t = \tau$  and  $t = \tau - 900$  as. The minus sign results from the delay definition used.

In the simulations, this propagation effect is not directly included. In order to take it into account, the theoretical signal has to be averaged by

$$\Delta\tilde{\epsilon}(E, \tau) = \frac{1}{\Delta T} \int_{\tau-\Delta T}^{\tau} \Delta\epsilon(E, t) dt, \quad (\text{S9})$$

with  $\Delta T$  equal to 900 as.  $\Delta\epsilon(E, t)$  is the change of the dielectric function simulated with the *ab-initio* and three-band models, respectively. As illustrated in Fig. S7, the averaging has an important effect onto the signal. With neglected propagation, the offset between the experimental and the simulated trace is approximately 600 as. Taking the propagation into account results in a reduced phase offset of below 250 as. The residual offset between the experiment and simulation might result from the longitudinal dependence of the non-uniform IR field distribution in the bulk material. As described above, we include the macroscopic propagation in a simplified way by averaging the signal (Eq. 9). It is however important to note that taking propagation into account results mainly in a shift of the energy dispersion shown in Fig. 3(f) of the main manuscript along the delay axis without any significant change to its shape. All simulations shown in the main manuscript take the propagation effects according to equation (S9) into account.

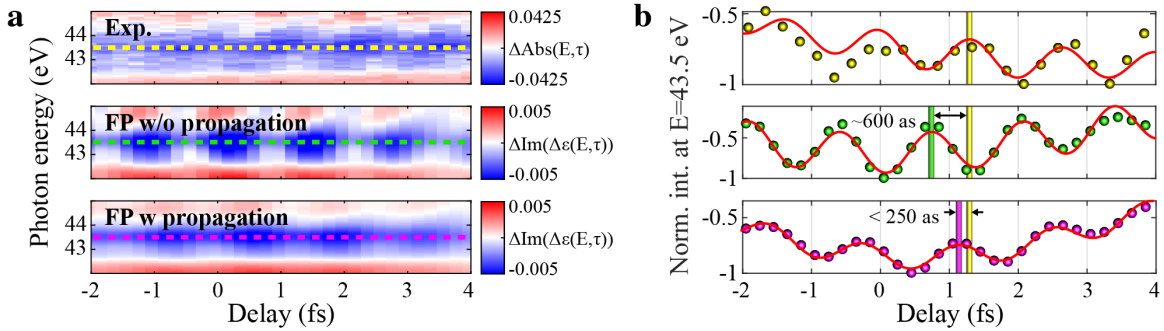


**Fig. S7. Propagation effect.** (a) Comparison of the experimental signal (upper) with the first-principles simulation without (middle) and with (lower) propagation included. (b) Energy averaged signal around 43.5 eV for the three traces in (a) (integration width of 0.2 eV). The vertical lines compare the individual peak positions. As we can see, taking the propagation into account results in a significant reduction of the phase offset between the experiment and simulation.

### S2.3 Pump intensity dependence

Studying the dependence of the ATAS signal on varying IR pump intensity experimentally is challenging. Reducing the pump intensity results in a significantly weaker signal and is limited by the achievable signal-to-noise ratio. Increasing it leads to irreversible damage of the membrane. The experimental traces presented in the main manuscript are recorded with an IR pump intensity close to the damage threshold of the GaAs target.

Nevertheless, to study the intensity-scaling of the signal, we performed first-principles simulations with varying IR-pump intensity. First, we computed the number of carriers injected by the pump (see section S1.4). Figure S2 shows the carrier population as a function of the laser intensity. One can clearly see the nonlinearity of the carrier injection mechanism. Second, we performed simulations of the transient absorption with different pump intensities. Figure S8 shows two example traces for  $5 \times 10^{11} \text{ W/cm}^2$  and  $1 \times 10^{12} \text{ W/cm}^2$ . Reducing the pump intensity results in a smaller absorption change. However, the shape is preserved. This fact indicates that the modification of the optical properties has a linear dependence on the laser intensity, while the carrier injection mechanism has a nonlinear dependence. This is consistent with our finding that the transient modification of the optical property is dominated by the virtual carrier effect of the intra-band transition, which scales linearly, while the carrier-injection is enhanced by the coupling of the intra- and inter-band transition, which scales nonlinearly.

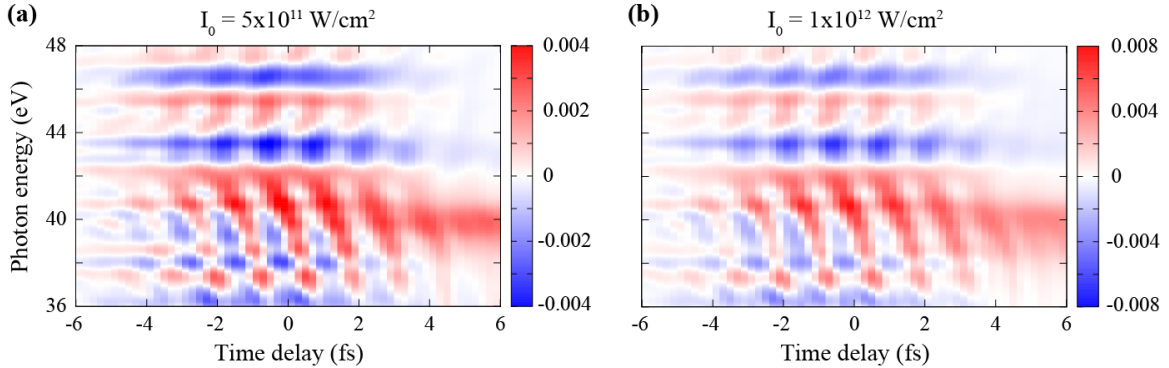


**Fig. S8. First-principles simulation of absorption modulation for two IR pump intensities. (a)  $5 \times 10^{11} \text{ W/cm}^2$ . (b)  $1 \times 10^{12} \text{ W/cm}^2$ .**

## S2.4 Probe-decomposition based on Houston states

The first-principles calculations with the propagation effects reproduce the experimental result very well. In order to clarify the microscopic origin of the signal, it is helpful to apply a probe-decomposition based on Houston states<sup>10</sup>.

For the decomposition, we first consider a decomposition of the full Hamiltonian into the pump and the probe part:  $\hat{H}_{pump-probe} = \hat{H}_{pump} + \hat{H}_{probe}$ .  $\hat{H}_{pump-probe}$  is the one-body Hamiltonian in equation (S8), while  $\hat{H}_{pump}$  is the Hamiltonian only including the pump pulse. The probe part,  $\hat{H}_{probe}$ , is defined by the difference of  $\hat{H}_{pump-probe}$  and  $\hat{H}_{pump}$ .

Next, we consider the matrix representation of the probe Hamiltonian based on the instantaneous eigenstates  $u_{bk}^P(\mathbf{r}, t)$  of the pump Hamiltonian, also known as Houston states<sup>25,41</sup>,

$$\left[ \frac{1}{2m} \left\{ \mathbf{p} + \hbar \mathbf{k} + \frac{e}{c} \mathbf{A}_{pump}(t) \right\}^2 + v(\mathbf{r}) \right] u_{bk}^P(\mathbf{r}, t) = \varepsilon_{bk + \frac{e}{\hbar c} \mathbf{A}_{pump}(t)} u_{bk}^P(\mathbf{r}, t). \quad (\text{S10})$$

Finally, by partially including/omitting the matrix elements of the probe Hamiltonian in the simulation, we can investigate dynamics induced by a specific probe transition. It is important to note that the pump mechanism is not influenced by the probe decomposition discussed here. Only the probe transitions between different energy levels are modified.

Figure S9 illustrates the probe decomposition of the first-principles simulation. As we can see, the full signal (Fig. S9(a)) is almost perfectly reproduced by the decomposed signal when including only the probe transition from the As-3*d* core level to the VB and CB (Fig. S9(b)). The transient signal in this energy regime is therefore dominated by probe transitions involving the As-3*d* core level as expected.

For a more detailed understanding, we further decompose the first-principles signal into the CB (Fig. S9(c)) and the VB response (Fig. S9(d)). In these cases, only probe transitions from the core level to either the CB or VB are allowed. One can see that the transient features in the absorption around 43 eV come mainly from probe transition between the As-3*d* level and the CB. Based on this, we focus on the CB response in the following analysis using the three-band model.

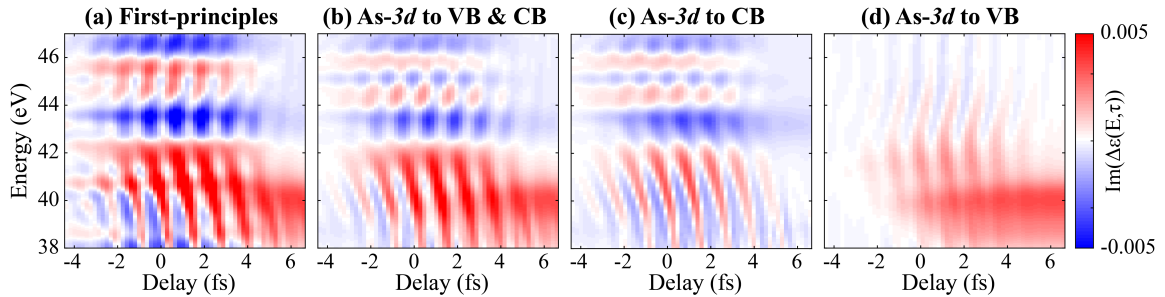


**Fig. S9. Decomposition of the first-principles signal.** (a) Full signal without any decomposition. (b) Decomposed signal with probe transitions from As-3*d* bands to valence and conduction bands, (c) from As-3*d* to only conduction bands (CB response), and (d) from As-3*d* to only valence bands (VB response).



## S2.5 Simplified 3-band model

To investigate the role of *intra*- and *inter*-band transitions in the transient response of GaAs, we employ a simple model consisting of only three bands: A flat band, which mimics the As-3*d* core level, and two parabolic bands representing the VB and CB. We set the energy level of the As-3*d* band to -40.73 eV with respect to the VB edge<sup>30</sup>. The band gap is  $\varepsilon_{gap} = 1.52$  eV, which is equal to the band gap of GaAs at zero Kelvin<sup>29</sup>. The shape of the parabolic bands is given by the corresponding effective electron masses ( $m_{CB} = 0.067 m_e$ <sup>29</sup>,  $m_{lh,VB} = 0.08 m_e$ <sup>42</sup>). For the VB, we choose the light-hole mass rather than the heavy-hole mass, as the simulation with this choice reproduces the experiment better (see Section S2.5.2).

Based on the above assumptions, one can consider the following Houston expansion<sup>41</sup> with three instantaneous eigenstates of the time-dependent Hamiltonian for each crystal momentum,

$$u_{\mathbf{k}}(\mathbf{r}, t) = c_{dk}(t)u_{dk}^H(\mathbf{r}, t) + c_{vk}(t)u_{vk}^H(\mathbf{r}, t) + c_{ck}(t)u_{ck}^H(\mathbf{r}, t), \quad (\text{S11})$$

where  $u_{dk}^H(\mathbf{r}, t)$ ,  $u_{vk}^H(\mathbf{r}, t)$  and  $u_{ck}^H(\mathbf{r}, t)$  are the instantaneous eigenstates of the As-3*d* level, VB and CB, respectively. The dynamics of the three-band model is described by the following Schrödinger equation for the time-dependent coefficients:

$$i\hbar \frac{\partial}{\partial t} \begin{pmatrix} c_{dk}(t) \\ c_{vk}(t) \\ c_{ck}(t) \end{pmatrix} = \begin{pmatrix} \varepsilon_d & h_{dv, \mathbf{K}(t)} & h_{dc, \mathbf{K}(t)} \\ h_{dv, \mathbf{K}(t)}^* & \varepsilon_{v, \mathbf{K}(t)} & h_{vc, \mathbf{K}(t)} \\ h_{dc, \mathbf{K}(t)}^* & h_{vc, \mathbf{K}(t)}^* & \varepsilon_{c, \mathbf{K}(t)} \end{pmatrix} \begin{pmatrix} c_{dk}(t) \\ c_{vk}(t) \\ c_{ck}(t) \end{pmatrix}, \quad (\text{S12})$$

where the crystal momentum  $\hbar \mathbf{K}(t)$  is shifted by the vector field,  $\hbar \mathbf{K}(t) = \hbar \mathbf{k} + \mathbf{A}(t) / c$ .

The matrix elements are defined as:

$$\varepsilon_{v, \mathbf{K}(t)} = -\frac{\mathbf{K}(t)^2}{2m_{lh, VB}}, \quad \varepsilon_{c, \mathbf{K}(t)} = \varepsilon_{gap} + \frac{\mathbf{K}(t)^2}{2m_{CB}}, \quad \varepsilon_d = -40.73 \text{ eV}, \quad (\text{S13})$$

$$h_{ij, \mathbf{K}(t)} = -i\mathbf{p}_{ij} \cdot \frac{\mathbf{E}(t)}{(\varepsilon_{i, \mathbf{K}(t)} - \varepsilon_{j, \mathbf{K}(t)})}. \quad (\text{S14})$$

The diagonal elements of the 3x3 matrix describe the electronic structure of the three-band model with the energy levels and effective masses introduced above. The off-

diagonal elements are defined by the corresponding momentum matrix elements,  $p_{ij}$ . To investigate the probe-induced transition from the semi-core to the CB in the main manuscript (CB response), we set  $p_{dv}$  to zero. Here, we note that the momentum matrix element between the *As-3d* band and the CB,  $p_{dc}$ , does not have any effect on the structure of the induced signal since there is no nonlinear effect from the semi-core transition at the present laser intensity. It only affects the absolute value of the signal.

In order to further construct the model, we need to define the momentum matrix element between the VB and CB,  $p_{vc}$ . For this purpose, we compute the signal with the three-band model for different values of the matrix element. Figure S10 compares the corresponding energy-averaged signals (integration interval: 42.5 to 43.0 eV) with the *ab-initio* simulation. The black-solid line follows the signal extracted from the first-principles calculation. The other lines show the signals of the three-band model for different values of the matrix element. As seen from the figure, a squared matrix element  $p_{vc}^2$  of 0.02 a.u. reproduces the first-principles simulation best, especially the ratio of the transient and long-lasting signal. Therefore, we chose this value for the three-band model simulations shown in the main manuscript.

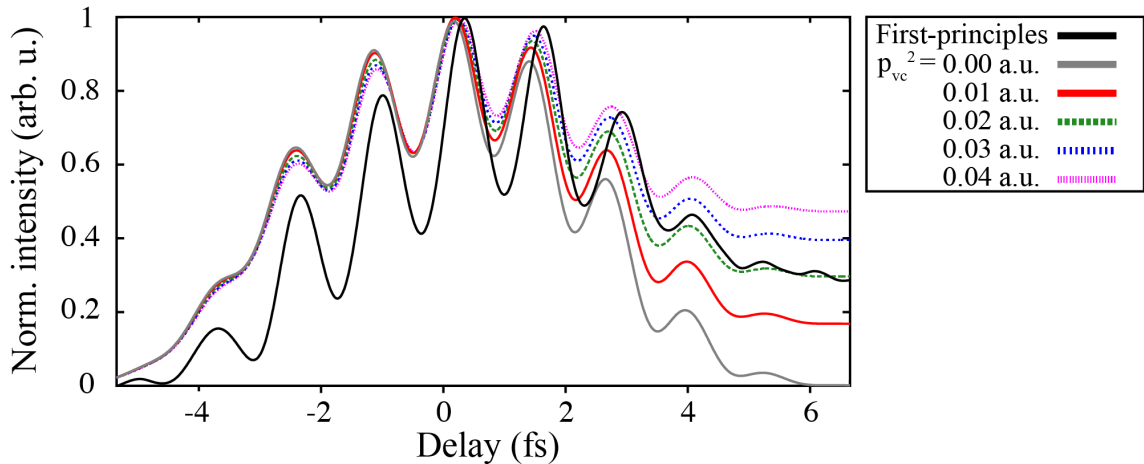


**Fig. S10. Extraction of matrix element  $p_{vc}$ .** Here, the energy-averaged signals (integration interval: 42.5 to 43 eV) extracted from the first-principles calculation and three-band model simulations for different matrix elements are compared. A value of  $p_{vc}^2=0.02$  a.u. reproduces the first-principles simulation best.

### S2.5.1 Intra- and inter-band limit

The advantage of this three-band model is that *intra*-band and *inter*-band transitions are described by different matrix elements of the Hamiltonian in equation (S12). On one hand, *intra*-band motion is described by the modification of the single-particle energy levels, which are given by the diagonal elements. The change of the energies is due to the crystal momentum shift,  $\hbar\mathbf{K}(t) = \hbar\mathbf{k} + \mathbf{A}(t)/c$ . On the other hand, *inter*-band transitions are described via off-diagonal elements. In the main text, we investigate the *intra*-band transition limit by neglecting the off-diagonal elements in the Hamiltonian (Fig. 3(c) of the main manuscript) and the *inter*-band transition limit by neglecting the modification of the single-particle energies (Fig. 3(d) of the main manuscript).

### S2.5.2 Heavy-hole valence band

As mentioned above, we assume the light-hole mass for the VB in the three-band model calculations. To justify our choice, we compare here the response of the model with the (a) light-hole VB and (b) heavy-hole VB. To investigate the VB response, we set the matrix element between core level and CB,  $p_{dc}$ , to zero.

As was done for the light-hole band, we find the momentum matrix element  $p_{vc}$  for the heavy-hole band, which reproduces the first-principles result best. We find that a  $p_{vc}^2$  of 0.01 a.u. yields the best match. Figure S11 shows the VB response computed for both, light-hole and heavy-hole, cases. By comparison with the corresponding decomposition of the first-principles signal (Fig. S9(d)), one finds that the signal with the light-hole band yields a better agreement; i.e., it reproduces correctly the wider distribution in the long-lasting component, and the V-shaped structure in the transient signal.

Based on this analysis, we chose the light-hole band instead of the heavy-hole band in the three-band simulations.

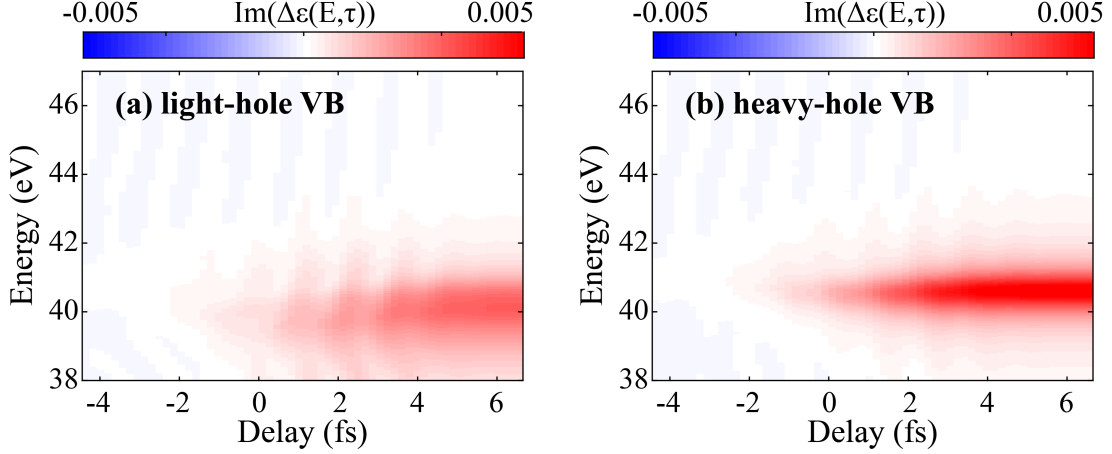


**Fig. S11.** Comparison of the valence band responses from a three-band model including (a) a light-hole and (b) a heavy-hole valence band, respectively.

### S2.5.3 Conduction band population

The population of the CB discussed in the main manuscript is defined by the projection of the time-dependent wave function  $u_{\mathbf{k}}(\mathbf{r}, t)$  onto the instantaneous eigenstate of the CB,

$u_{c_{\mathbf{k}}}^H(\mathbf{r}, t)$ :

$$n_{CB}(t) = \frac{2}{(2\pi)^3} \int d\mathbf{k} \left| \langle u_{c_{\mathbf{k}}}^H(t) | u_{\mathbf{k}}(t) \rangle \right|^2 = \frac{2}{(2\pi)^3} \int d\mathbf{k} |c_{c_{\mathbf{k}}}(t)|^2, \quad (\text{S15})$$

where  $c_{c_{\mathbf{k}}}(t)$  is the CB coefficient derived from equation (S12). To investigate only the population dynamics between VB and CB in Fig. 4 of the main manuscript, we set both  $p_{dv}$  and  $p_{dc}$  to zero.

### S2.6 Spin-orbit splitting

The As- $3d$  core level is divided into the  $3d_{5/2}$  and  $3d_{3/2}$  states due to the spin-orbit splitting. The level separation is  $0.68 \text{ eV}^{43}$ . As the probe pulse can excite electrons from both core levels to the bandgap region, the measured signal can actually be seen as a superposition of two ATAS traces. In our simulations, no splitting is taken into account. Only one core level lying  $40.73 \text{ eV}$  below the valence band maximum is included<sup>30</sup>. To estimate the influence of the splitting on the calculated signal, we can look at

$$\Delta\varepsilon_{so}(E, \tau) = 6 \cdot \text{Im}(\Delta\varepsilon(E + \frac{\Delta E_{so}}{2}, \tau)) + 4 \cdot \text{Im}(\Delta\varepsilon(E - \frac{\Delta E_{so}}{2}, \tau)), \quad (\text{S16})$$

where  $\Delta\varepsilon(E, \tau)$  is the simulated change of the dielectric function without splitting.  $E$  and

$\tau$  describe the energy and delay dependence.  $\Delta E_{SO}$  is the energy splitting of the core levels. The pre-factors 6 and 4 represent the degeneracy of the two core levels. By comparing the first-principles calculations without (Fig. S12(a)) and with (Fig. S12(b)) the splitting included, one finds that the core level splitting does not have a significant influence on the main features of the transient and long-lasting signal. It mainly results in an energy averaging. Therefore, we neglected the spin-orbit splitting in all calculations shown in this manuscript.

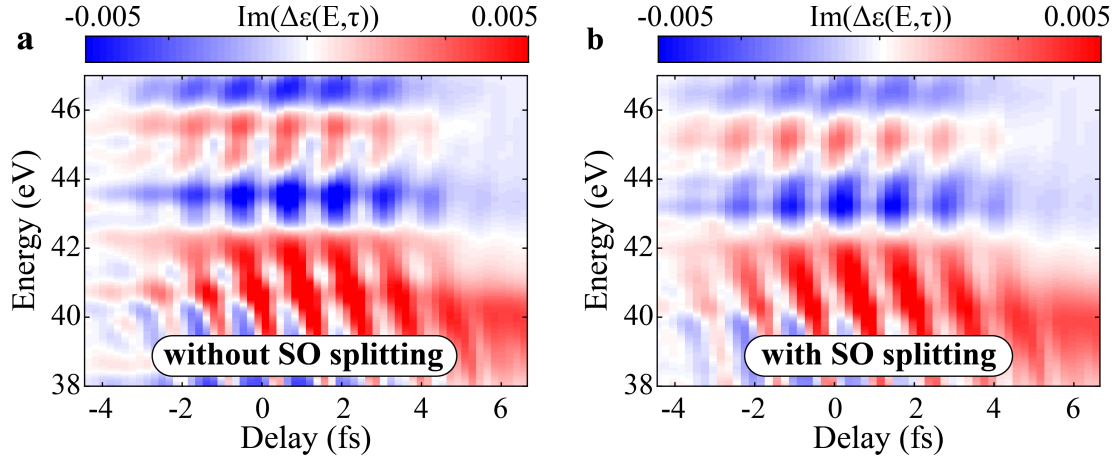


**Fig. S12. Influence of core-level splitting.** First-principles simulation (a) without and (b) with included spin-orbit splitting of the As-3d core level. As one can see, the splitting results only in an energy averaging of the signal without any significant influence on the main features.

## S2.7 Multi-photon resonant pump regime

Using our simplified 3-band model, we calculated the number of carriers excited into the conduction band of GaAs ( $E_{gap} = 1.52$  eV) for the case of a multi-photon resonant pump pulse. The pump photon energy used in the following is  $1.52/3$  eV. The pump intensity has been set to  $10^{10}$  W/cm<sup>2</sup>. The corresponding Keldysh parameter is  $\sim 1.55$ , which suggests that multi-photon excitation is more likely to occur than tunneling excitation.

In Fig. S13, we show the corresponding conduction band population for the full model, including both transition types, and for the inter-band-only case on a linear (a) and logarithmic (b) axis. As in the resonant pump regime, we can clearly see that including intra-band motion results in an enhanced injection rate.

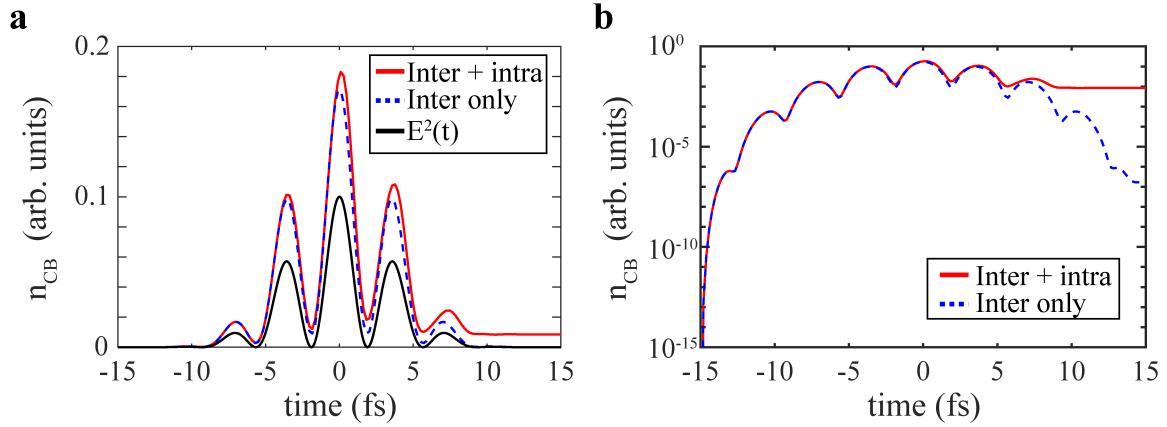


**Fig. S13.** Number of carriers excited into the conduction band of GaAs by a 3-photon resonant pump pulse. The black solid line in (a) illustrates the temporal shape of the pump intensity. Including intra-band motion into the simulations results in an enhancement of the number of excited carriers as in the single-photon resonant pump regime. In (b), the CB population is plotted on a logarithmic scale.

## References

- 1 Mei, X. *et al.* First Demonstration of Amplification at 1 THz Using 25-nm InP High Electron Mobility Transistor Process. *IEEE Electron Device Letters* **36**, 327-329 (2015).
- 2 Desai, S. B. *et al.* MoS<sub>2</sub> transistors with 1-nanometer gate lengths. *Science* **354**, 99-102 (2016).
- 3 Krausz, F. & Stockman, M. I. Attosecond metrology: from electron capture to future signal processing. *Nat. Photon.* **8**, 205-213 (2014).
- 4 Schultze, M. *et al.* Attosecond band-gap dynamics in silicon *Science* **346**, 1348-1352 (2014).
- 5 Mashiko, H., Oguri, K., Yamaguchi, T., Suda, A. & Gotoh, H. Petahertz optical drive with wide-bandgap semiconductor. *Nat. Phys.* **12**, 741-745 (2016).
- 6 Sommer, A. *et al.* Attosecond nonlinear polarization and light-matter energy transfer in solids. *Nature* **534**, 86-90 (2016).
- 7 Zürich, M. *et al.* Ultrafast carrier thermalization and trapping in silicon-germanium alloy probed by extreme ultraviolet transient absorption spectroscopy. *Structural Dynamics* **4**, 044029 (2017).
- 8 Zürich, M. *et al.* Direct and simultaneous observation of ultrafast electron and hole dynamics in germanium. *Nature Communications* **8**, 15734 (2017).
- 9 Schultze, M. *et al.* Controlling dielectrics with the electric field of light. *Nature* **493**, 75-78 (2013).
- 10 Lucchini, M. *et al.* Attosecond dynamical Franz-Keldysh effect in polycrystalline diamond. *Science* **353**, 916 - 919 (2016).
- 11 Golde, D., Meier, T. & Koch, S. W. High harmonics generated in semiconductor nanostructures by the coupled dynamics of optical inter- and intraband excitations. *Phys. Rev. B* **77**, 075330 (2008).
- 12 Ghimire, S. *et al.* Observation of high-order harmonic generation in a bulk crystal. *Nat. Phys.* **7**, 138-141 (2011).
- 13 Malard, L. M., Mak, K. F., Castro Neto, A. H., Peres, N. M. R. & Heinz, T. F. Observation of intra- and inter-band transitions in the transient optical response of graphene. *New J. Phys.* **15**, 015009 (2013).
- 14 Al-Naib, I., Sipe, J. E. & Dignam, M. M. High harmonic generation in undoped graphene: Interplay of inter- and intraband dynamics. *Phys. Rev. B* **90**, 245423 (2014).
- 15 Luu, T. T. *et al.* Extreme ultraviolet high-harmonic spectroscopy of solids. *Nature* **521**, 498-502 (2015).
- 16 Wismer, M. S., Kruchinin, S. Y., Ciappina, M., Stockman, M. I. & Yakovlev, V. S. Strong-Field Resonant Dynamics in Semiconductors. *Phys. Rev. Lett.* **116**, 197401 (2016).
- 17 Paasch-Colberg, T. *et al.* Sub-cycle optical control of current in a semiconductor: from the multiphoton to the tunneling regime. *Optica* **3**, 1358 (2016).
- 18 Ludwig, A. *et al.* Breakdown of the Dipole Approximation in Strong-Field Ionization. *Phys. Rev. Lett.* **113**, 243001 (2014).
- 19 Locher, R. *et al.* Versatile attosecond beamline in a two-foci configuration for simultaneous time-resolved measurements. *Rev. Sci. Instrum.* **85**, 013113 (2014).

- 20 Hentschel, M. *et al.* Attosecond metrology. *Nature* **414**, 509-513 (2001).
- 21 Itatani, J. *et al.* Attosecond Streak Camera. *Phys. Rev. Lett.* **88**, 173903 (2002).
- 22 Schlaepfer, F. *et al.* Gouy phase shift for annular beam profiles in attosecond experiments. *Opt. Express.* **25**, 3646-3655 (2017).
- 23 Beard, M. C., Turner, G. M. & Schmuttenmaer, C. A. Transient photoconductivity in GaAs as measured by time-resolved terahertz spectroscopy. *Phys. Rev. B* **62**, 15764 - 15777 (2000).
- 24 Sato, S. A., Yabana, K., Shinohara, Y., Otobe, T. & Bertsch, G. F. Numerical pump-probe experiments of laser-excited silicon in nonequilibrium phase. *Phys. Rev. B* **89**, 064304 (2014).
- 25 Houston, W. V. Acceleration of Electrons in a Crystal Lattice. *Physical Review* **57**, 184-186 (1940).
- 26 Srivastava, A., Srivastava, R., Wang, J. & Kono, J. Laser-Induced Above-Band-Gap Transparency in GaAs. *Phys. Rev. Lett.* **93**, 157401 (2004).
- 27 Novelli, F., Fausti, D., Giusti, F., Parmigiani, F. & Hoffmann, M. Mixed regime of light-matter interaction revealed by phase sensitive measurements of the dynamical Franz-Keldysh effect. *Sci. Rep.* **3**, 1227 (2013).
- 28 Bakos, J. S. AC stark effect and multiphoton processes in atoms. *Phys. Rep.* **31**, 209-235 (1977).
- 29 Vurgaftman, I., Meyer, J. R. & Ram-Mohan, L. R. Band parameters for III-V compound semiconductors and their alloys. *J. Appl. Phys.* **89**, 5815-5875 (2001).
- 30 Kraut, E. A., Grant, R. W., Waldrop, J. R. & Kowalczyk, S. P. Precise Determination of the Valence-Band Edge in X-Ray Photoemission Spectra: Application to Measurement of Semiconductor Interface Potentials. *Phys. Rev. Lett.* **44**, 1620-1623 (1980).
- 31 Sola, I. J. *et al.* Controlling attosecond electron dynamics by phase-stabilized polarization gating. *Nat. Phys.* **2**, 319-322 (2006).
- 32 Harris, J. G. E., Awschalom, D. D., Maranowski, K. D. & Gossard, A. C. Fabrication and characterization of 100 - nm - thick GaAs cantilevers. *Rev. Sci. Instrum.* **67**, 3591-3593 (1996).
- 33 Liu, J. *et al.* High-Q optomechanical GaAs nanomembranes. *Appl. Phys. Lett.* **99**, 243102 (2011).
- 34 Aspnes, D. E. & Studna, A. A. Dielectric functions and optical parameters of Si, Ge, GaP, GaAs, GaSb, InP, InAs, and InSb from 1.5 to 6.0 eV. *Phys. Rev. B* **27**, 985-1009 (1983).
- 35 Lucchini, M. *et al.* Ptychographic reconstruction of attosecond pulses. *Opt. Express.* **23**, 29502-29513 (2015).
- 36 Runge, E. & Gross, E. K. U. Density-Functional Theory for Time-Dependent Systems. *Phys. Rev. Lett.* **52**, 997-1000 (1984).
- 37 Hirokawa, Y., Boku, T., Sato, S. A. & Yabana, K. in *2016 IEEE International Parallel and Distributed Processing Symposium Workshops (IPDPSW)*. 1202-1211.
- 38 Tran, F. & Blaha, P. Accurate Band Gaps of Semiconductors and Insulators with a Semilocal Exchange-Correlation Potential. *Phys. Rev. Lett.* **102**, 226401 (2009).
- 39 Koller, D., Tran, F. & Blaha, P. Improving the modified Becke-Johnson exchange potential. *Phys. Rev. B* **85**, 155109 (2012).



- 40 Sato, S. A. & Yabana, K. Efficient basis expansion for describing linear and  
nonlinear electron dynamics in crystalline solids. *Phys. Rev. B* **89**, 224305 (2014).
- 41 Krieger, J. B. & Iafrate, G. J. Time evolution of Bloch electrons in a  
homogeneous electric field. *Phys. Rev. B* **33**, 5494-5500 (1986).
- 42 Yu, P. Y. & Cardona, M. *Fundamentals of Semiconductors*. (Springer Verlag,  
1996).
- 43 van der Veen, J. F., Smit, L., Larsen, P. K. & Neave, J. H. Core level binding  
energy shifts for reconstructed GaAs(001) surfaces. *Physica B+C* **117**, 822-824  
(1983).